ON THE NUMERICAL SIMULATION OF HYPERBOLIC HEAT CONDUCTION USING HIGH ORDER WENO

Tamer Kasem*, Adel Mohsen

Department of Engineering Mathematics and Physics, Faculty of Engineering, Cairo University, Giza, 12613, Egypt

Keywords: Hyperbolic heat transfer, Finite difference, WENO, High order methods, wide stencils

ABSTRACT

Numerical simulation of hyperbolic heat conduction is performed using the high order accurate weighted essentially non-oscillatory (WENO) method. Algorithms for imposing Neumann and Dirichlet boundary conditions, in the presence of wide stencils are clarified. The results are validated via comparison with exact solutions. The sharp gradients induced by thermal waves are accurately reproduced. The results verify that the error (E) is inversely proportional to the number of grid points (N) and the order of the method (k). To quantify the benefit of increasing k, the ratio between the grid sizes of $k=9$ and $k=5$ simulations, yielding the same E is obtained. It is found that increasing k is more economic (i.e. lower N is needed) in the transient interval characterized by strong discontinuities, compared to the steady interval.

1. Introduction

Generally macroscale heat transfer is governed by the Fourier law. This law states that heat is transferred only by diffusion. However as the dimensions of physical devices shrink and the response time shortens various physical phenomena arise [1]. The reason is the relatively small size of the control volume. This volume which contains hundreds or thousands of lattices in the macroscale problems, contains only a few energy carriers in the microscale problems. One of the models which may be used at microscale levels is the thermal wave (hyperbolic) model [2], [3], [4].

The basic feature of the hyperbolic model is the finite signal propagation speed. This feature leads to thermal distributions with discontinuities and sharp gradients. These sharp gradients were illustrated by the exact solutions provided in [5], [6] and [7]. However, special numerical methods are needed for cases involving sharp gradients. For example, increasing the order of space space discretization (k) near discontinuities may lead to spurious oscillations resulting from Gibbs phenomenon [8]. Although low order numerical methods $(k<2)$ can yield stable solutions, the results may suffer from extra diffusion. This topic was investigated by Yang in [9]. He clarified the excessive diffusion induced by the upwind scheme $(k=1)$. He also illustrated the spurious oscillations resulting from Lax-Wendroff method $(k=2)$. As a remedy he suggested using second order Total Variation Diminishing (TVD) method to circumvent both disadvantages.

However, much progress has been achieved later regarding developing even higher order $(k>2)$ stable numerical algorithms. For example Balsara and Shu in [10] studied the high order space accurate weighted essentially non-oscillatory (WENO) method. They showed that $k=9$ can yield better resolution and accuracy for the same number of grid points (N), compared to $k=5$ algorithm. Later Shi et al. in [11] simulated hyperbolic compressible inviscid flow. They presented a qualitative comparison of the results of WENO adopting $k=5$ and $k=9$. They concluded that the same resolution of $k=5$, can be fulfilled adopting $k=9$ while reducing N by 50% in each direction. Consequently it is expected that using a high order method (HOM) is more economic concerning N.

*Corresponding author

E-mail address: tamerkasem@eng.cu.edu.eg

Tel: +20-2-3567-8063 (office) +20-111-5066-113 (cellular)

Recently applications of HOMs to hyperbolic heat transfer problems were investigated. These works include; [12] where up to $k=5$ space-time discontinuous finite element was applied, and [2] where $k=5$ WENO method was used. Unfortunately in both studies a quantitative assessment of the reduction in N upon increasing k was not provided. Consequently the aim of this study is to provide this assessment.

The current literature is rich with various HOMs, and the interested reader can consult [13] for an extensive review. However among a wide variety of methods, WENO method enjoys several advantages. Extensive literature exists which is dedicated to developing high order versions of WENO including [10] where up to $k=11$ schemes were presented, and [14] where up to $k=17$ algorithms were developed. In addition WENO was applied successfully to various problems [8]. The current work focuses on $k=5$ and $k=9$ WENO algorithms due to their importance.

A major feature of WENO is that the stencil size is proportional to k. The presence of this wide stencil renders imposing the correct boundary conditions as a non trivial task. A goal of this study is clarifying this task.

2. Governing equations

The Energy balance equation for purely thermal response is given by:

$$\rho C_P \frac{\partial T}{\partial t} + \nabla \cdot \boldsymbol{q} = 0 \tag{1}$$

Here ρC_P is the volumetric heat capacity, T is the temperature field and $\boldsymbol{q}$ is the heat flux vector. In case of Fourier heat transfer $\boldsymbol{q}$ is related to T by the constitutive relation:

$$\boldsymbol{q} = -\kappa \nabla T \tag{2}$$

where κ is the thermal conductivity. In case of hyperbolic heat transfer an additional material parameter, the thermal relaxation time τ is introduced as:

$$\tau \frac{\partial \boldsymbol{q}}{\partial t} + \boldsymbol{q} = -\kappa \nabla T \tag{3}$$

Using the dimensionless variables: $\nabla^* = L\nabla$, $T^* = T/T_0$, $t^* = \frac{t}{L^2/\alpha}$ and $\boldsymbol{q}^* = \frac{\boldsymbol{q}}{\kappa T_0/L}$, defined in terms of the reference length L , the reference temperature T_0 and the thermal diffusivity $\alpha = \kappa/(\rho C_P)$, Eqs. (1) and (3) are written as:

$$\frac{\partial T^*}{\partial t^*} + \nabla^* \cdot \boldsymbol{q}^* = 0 \tag{4}$$

$$Ve^2 \frac{\partial \boldsymbol{q}^*}{\partial t^*} + \boldsymbol{q}^* = -\nabla^* T^* \tag{5}$$

Here Ve is the Vernotte number [7] defined as $Ve^2 = \frac{\alpha\tau}{L^2}$. Omitting the * superscripts for convenience, Eqs. (4) and (5) can be written in the one-dimensional form as:

$$\begin{bmatrix} T \\ q \end{bmatrix}_t + \begin{bmatrix} q \\ \frac{T}{Ve^2} \end{bmatrix}_x = \begin{bmatrix} 0 \\ -q/Ve^2 \end{bmatrix} \tag{6}$$

Here the subscripts t and x denotes time and space partial differentiation, respectively. In order to clarify the characteristics of Eq. (6), we introduce the Jacobian matrix defined as:

$$[J]=\begin{bmatrix} 0 & 1 \\ 1/Ve^2 & 0 \end{bmatrix} \tag{7}$$

The hyperbolic system described by Eq. (6) can be rewritten using $[J]$ as:

$$\begin{bmatrix} T \\ q \end{bmatrix}_t + [J]\begin{bmatrix} T \\ q \end{bmatrix}_x = \begin{bmatrix} 0 \\ -q/Ve^2 \end{bmatrix} \tag{8}$$

In order to solve Eq. (8) numerically using WENO method, the diagonal matrix of eigen values $[\Lambda]$ of $[J]$, and the matrix $[R]$ whose columns are the corresponding eigen vectors, and $[R]^{-1}$ which is the inverse of $[R]$ should be obtained. These are given as:

$$[\Lambda]=\begin{bmatrix} 1/Ve & 0 \\ 0 & -1/Ve \end{bmatrix} \quad [R]=\begin{bmatrix} 1 & 1 \\ 1/Ve & -1/Ve \end{bmatrix} \quad [R]^{-1}=\begin{bmatrix} 1/2 & Ve/2 \\ 1/2 & -Ve/2 \end{bmatrix} \tag{9}$$

Although the numerical scheme in the current work will be applied to Eq. (6), it is useful to rewrite the equation in the characteristic form. To fulfill this task Eq. (8) is pre-multiplied by $[R]^{-1}$ and the identity $[R]^{-1}\begin{bmatrix} 0 & 1 \\ 1/Ve^2 & 0 \end{bmatrix}[R]=[\Lambda]$ is used. The result is:

$$\begin{bmatrix} W_1 \\ W_2 \end{bmatrix}_t + \begin{bmatrix} 1/Ve & 0 \\ 0 & -1/Ve \end{bmatrix}\begin{bmatrix} W_1 \\ W_2 \end{bmatrix}_x = \begin{bmatrix} -\dfrac{q}{2Ve} \\ \dfrac{q}{2Ve} \end{bmatrix} \tag{10}$$

Here the characteristic variables are defined as $\left[W_1 \ , \ W_2\right]=\left[\dfrac{T}{2}+Ve\dfrac{q}{2} \ , \ \dfrac{T}{2}-Ve\dfrac{q}{2}\right]$. Upon writing the governing equations in the characteristic form, the wave nature of the problem is clarified [2]. In fact two waves exist; W_1 moving from left to right with a speed $1/Ve$, and W_2 moving with the same speed in the opposite direction. The characteristic form is important for implementing Dirichlet boundary equation, as will be illustrated later.

3. Numerical algorithm

The details of WENO method are explained in [8]. Also formulas for the ninth order algorithm are provided in [10]. The solution steps are briefly described in this section. Although the algorithm will be presented for the uni-dimensional case, we note that extension to multidimensional cases is straightforward. A scalar one dimensional hyperbolic equation can be written as $u_t+f(u)_x=g(u)$ where u, $f(u)$ and $g(u)$ are the independent variable, the flux and the source term, respectively. The main goal is to provide a high order space discretization of the first order space derivative at a grid point i. This derivative is calculated as:

$$\frac{\partial f(u)}{\partial x}_i = \frac{\widehat{f}(u)_{i+\frac{1}{2}} - \widehat{f}(u)_{i-\frac{1}{2}}}{\Delta x} + O(\Delta x^k) \tag{11}$$

Here $\widehat{f}(u)_{i+\frac{1}{2}}$ is termed as the numerical flux, Δx is the grid spacing, and $k=2n-1$ is the order of discretization error. In fact $2n$ stencil points are needed to achieve a discretization error $O(\Delta x^k)$. In order to obtain entropy correct solutions "flux splitting" should be performed. In this process $\widehat{f}(u)_{i+\frac{1}{2}}$ is calculated as:

$$\widehat{f}(u)_{i+\frac{1}{2}} = \widehat{f}(u)^{+}_{i+\frac{1}{2}} + \widehat{f}(u)^{-}_{i+\frac{1}{2}} \tag{12}$$

Here $\widehat{f}(u)^{+}_{i+\frac{1}{2}}$ and $\widehat{f}(u)^{-}_{i+\frac{1}{2}}$ denote the downwind and the upwind fluxes, respectively. Adopting Local Lax-Friedrichs (LLF) scheme these fluxes are calculated as

$$\widehat{f}(u)^{\pm}_{i+\frac{1}{2}} = \frac{1}{2}\left(f(u) \pm \lambda u\right) \tag{13}$$

Here $\lambda = max\left(|\partial f(u)/\partial u|\right)$, where the maximum is evaluated over the $2n$ wide stencil. To clarify the algorithm, the numerical stencils of $\widehat{f}(u)^{\pm}_{i+\frac{1}{2}}$ for $k=5$ are shown in Fig. 1.

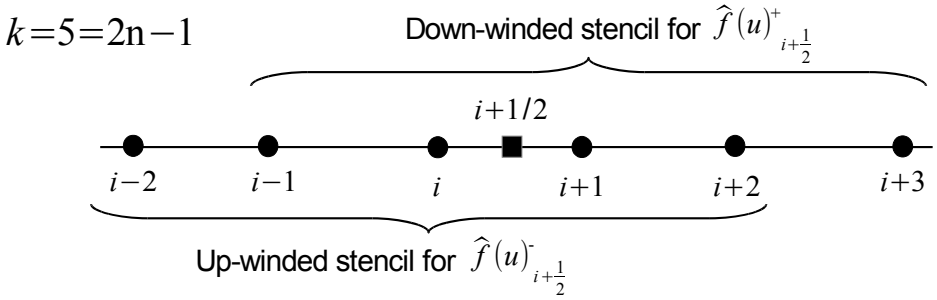

Fig. 1. Numerical stencils of $\widehat{f}(u)^{\pm}_{i+\frac{1}{2}}$

The full stencils of $\widehat{f}(u)^{\pm}_{i+\frac{1}{2}}$ are divided into n sub-stencils. For each sub-stencil j , a smoothness indicator IS_j is calculated. A weight is assigned to each sub-stencil that is inversely proportional to IS_j . $\widehat{f}(u)^{\pm}_{i+\frac{1}{2}}$ are evaluated as a weighted sum of estimates obtained from the n sub-stencils. In this way the effect of sub-stencils with sharp gradients is reduced, spurious oscillations are avoided, and high order solutions are obtained. For clarification the sub-stencils of $\widehat{f}(u)^{-}_{i+\frac{1}{2}}$ are shown in Fig. 2. The corresponding smoothness indicators are given as [8]:

$$\begin{aligned}
IS_0 &= \frac{13}{12}\left(f(u_{i-2}) - 2f(u_{i-1}) + f(u_i)\right)^2 + \frac{1}{4}\left(f(u_{i-2}) - 4f(u_{i-1}) + 3f(u_i)\right)^2 \\
IS_1 &= \frac{13}{12}\left(f(u_{i-1}) - 2f(u_i) + f(u_{i+1})\right)^2 + \frac{1}{4}\left(f(u_{i-1}) - f(u_{i+1})\right)^2 \\
IS_2 &= \frac{13}{12}\left(f(u_i) - 2f(u_{i+1}) + f(u_{i+2})\right)^2 + \frac{1}{4}\left(3f(u_i) - 4f(u_{i+1}) + f(u_{i+2})\right)^2
\end{aligned} \tag{14}$$

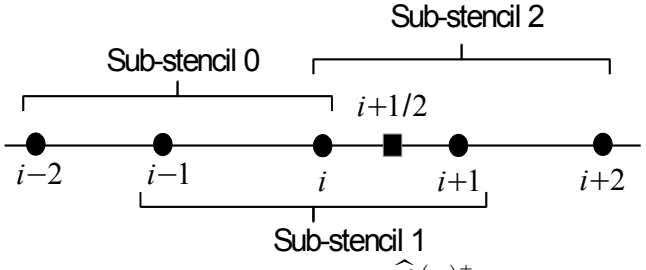

Fig. 2. Sub-stencils of $\widehat{f}(u)^{\pm}_{i+\frac{1}{2}}$

For systems of hyperbolic equations, the governing equation can be written as:

$$U_t + F(U)_x = G(U) \tag{15}$$

Here U , $F(U)$ and $G(U)$ are the vectors of independent variables, the flux and the source term, respectively. The eigen values and vectors of the system play two important roles. The first role is transforming the original coupled system to a diagonal uncoupled form. This is necessary since WENO algorithm is designed for scalar equations. The second role is in performing flux-splitting. In this case flux-splitting is performed separately for each characteristic variable, and $\lambda = max(|\Lambda_i|)$ where Λ_i is the corresponding eigen value. In fact, the numerical algorithm of WENO is applied to the $F(U)$ pre-multiplied by $[R]^{-1}$. The result is then multiplied by $[R]$ to obtain the numerical flux $\widehat{F}(u)_{i+\frac{1}{2}}$.

As already mentioned in the introduction, imposing boundary conditions in the presence of the relatively wide stencils is not a trivial task. For example three external fictitious points are needed at the domain boundaries for $k=5$. Implementing boundary conditions at these fictitious points will be detailed in the results section.

Time integration will be done using the optimal third order TVD Runge-Kutta method [8]. This method can be written as a series of three explicit time steps:

$$\begin{aligned} U^{(1)} &= U^n + \Delta t\left[-F(U^n)_x + G(U^n)\right] \\ U^{(2)} &= \frac{3}{4}U^n + \frac{1}{4}U^{(1)} + \frac{1}{4}\Delta t\left[-F(U^{(1)})_x + G(U^{(1)})\right] \\ U^{n+1} &= \frac{1}{3}U^n + \frac{2}{3}U^{(2)} + \frac{2}{3}\Delta t\left[-F(U^{(2)})_x + G(U^{(2)})\right] \end{aligned} \tag{16}$$

4. Results and discussion

In this section two cases of Neumann and Dirichlet boundary conditions will be studied. In order to clarify the numerical algorithm and its accuracy, the numerical and the exact solutions will be provided and compared for each case.

Case 1: Neumann Boundary Condition

Results of the numerical solution of Eq. (8) will be presented adopting Neumann boundary conditions. The results will be compared with the analytical solution given in [7]. The domain boundaries are located at $x=0$ and $x=1$. Zero space derivative boundary conditions are assigned for T .

$$\frac{\partial T}{\partial x}(x=0,t) = \frac{\partial T}{\partial x}(x=1,t) = 0 \tag{17}$$

Also the initial time derivative of the temperature is assigned to zero

$$\frac{\partial T}{\partial t}(x, t=0) = 0 \tag{18}$$

The symmetric nature of Eq. (17) implies that zero heat flux should be imposed at the boundaries.

$$q(x=0,t) = q(x=1,t) = 0 \tag{19}$$

The main factor governing the time response is the initial temperature distribution $T(x, t=0)$ which will be non-zero.

$$T(x, t=0) = H(x-0.25) - H(x-0.75) \tag{20}$$

Here $H(x)$ is the Heaviside step function.

Imposing zero boundary conditions on $\boldsymbol{q}$ and zero derivative boundary conditions on T is a

straightforward task even in the presence of a wide stencil. As shown in Fig. 3, values at fictitious boundary points are assigned using anti-symmetry for $\boldsymbol{q}$ and symmetry for T .

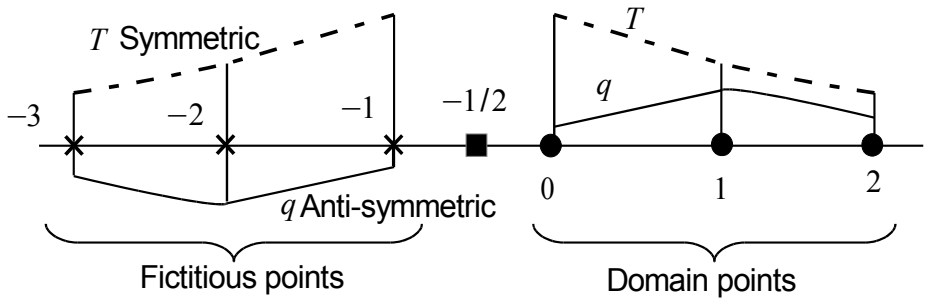

Fig. 3. Imposing boundary conditions at fictitious points for Neumann condition

The exact solution is given by [7]:

$$T = 0.5 + e^{\frac{-t}{2Ve^2}} \sum_{n=1}^{\infty} \left(A_n \cos(\alpha_n t) + B_n \sin(\alpha_n t) \right) \cos(n\pi x)$$

$$A_n = \frac{\sin(3n\pi/4) - \sin(n\pi/4)}{0.5 n\pi} \qquad B_n = \frac{A_n}{2Ve^2 \alpha_n} \qquad \alpha_n = \frac{\sqrt{4n^2\pi^2 Ve^2 - 1}}{2Ve^2} \tag{21}$$

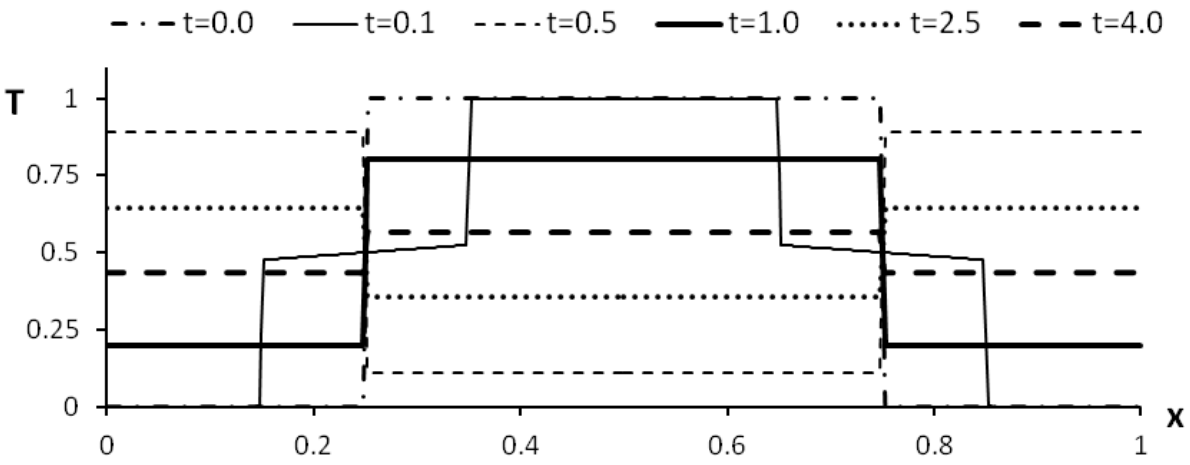

Fig. 4. Exact solution using Eq. (21) and adopting $Ve = 1$

The spatial temperature distribution is plotted in Fig. 4 at different instants adopting $Ve = 1$. The series summation in Eq. (21) is calculated using 20,000 terms. The main features of the solution are; the sharp gradients due to the initial distribution, reflection of the thermal wave from the boundaries, and the attenuation of the wave. The result of this attenuation is that, the solution approaches a space uniform value of 0.5 as $t \to \infty$.

The spatial temperature distribution at one instant ($t = 1.0$) is shown in Fig. 5, for various orders of numerical scheme ($k = 5$ and 9) and number of grid points ($N = 50$ and 100). It should be noted that $\Delta t = 1/(2N)$ for the all grids adopted. It is obvious from Fig. 5 that the accuracy is proportional to both k and N . In addition the advantage of avoiding spurious oscillations near sharp edges is illustrated.

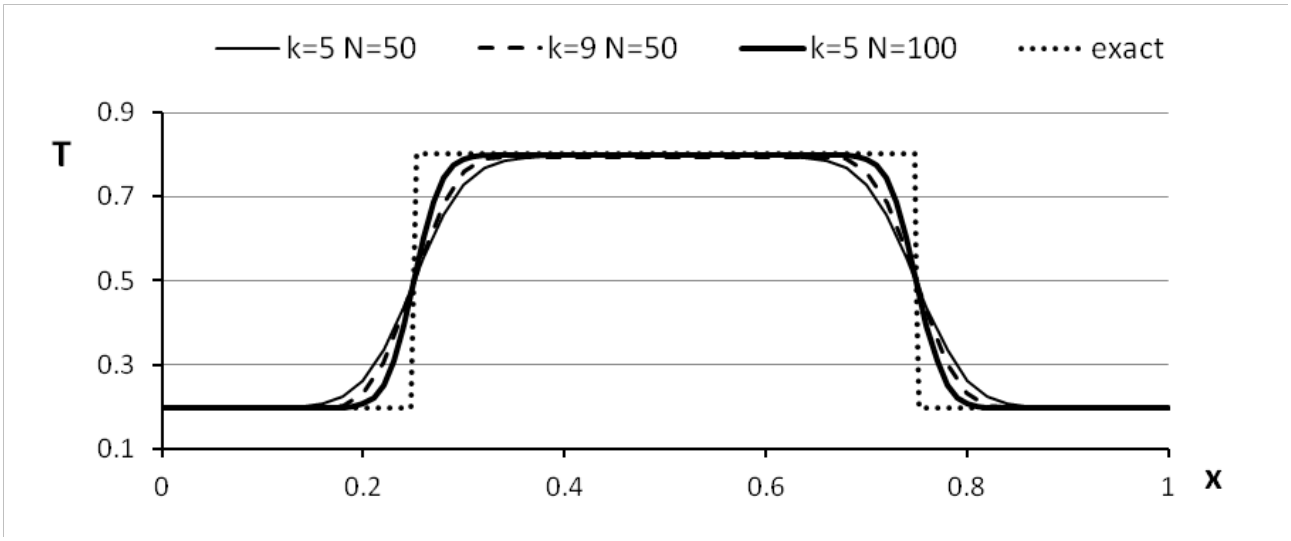

Fig. 5. Exact and numerical solution at $t=1.0$

On Fig. 6 the spatial distribution of the absolute error is shown for different values of k and N at the same instant of Fig. 5. It can be observed that the error increases near the sharp gradients. This is expected since the discontinuous zone is the most difficult feature to be modeled.

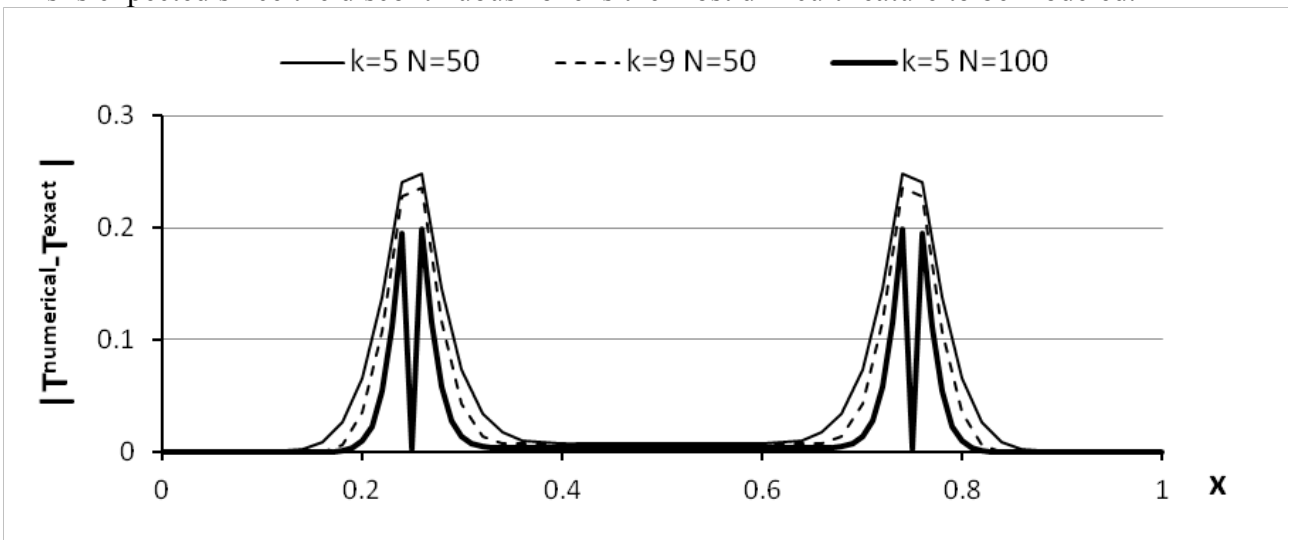

Fig. 6. Absolute error in temperature for various k *and* N *at* $t=1.0$

In order to clarify the temporal variation of the error, a quantitative estimate of the error at a certain instant is defined as

$$E=\frac{\sum_{i=0}^{N}\left|T_i^{\,exact}-T_i^{\,numerical}\right|}{N} \tag{22}$$

Here T_i is the temperature at grid point i. It should be noted that E is a zero order approximation of the error L_1 norm defined as [15]:

$$\|T^{exact}-T^{numerical}\|_1=\int_0^{1.0}\left|T^{exact}-T^{numerical}\right|dx \tag{23}$$

On Fig. 7 the variation of E at a fixed instant ($t=0.5$) is plotted versus N. Logarithmic scale is adopted for vertical and horizontal axis. The resulting plot is very close to a straight line for both values of k. Consequently the following formula is used to fit the data

$$E_k=a_k N_k^{\,b_k} \tag{24}$$

Here E_k is the error resulting of adopting k order accurate scheme, N_k is the number of grid points, a_k and b_k are constants to be obtained from least squares curve fitting. For example, on Fig. 7 the data are plotted along with the least squares fitted formula. The corresponding constants are $a_5=1.549$, $b_5=-0.933$, $a_9=1.6815$ and $b_9=-1.017$.

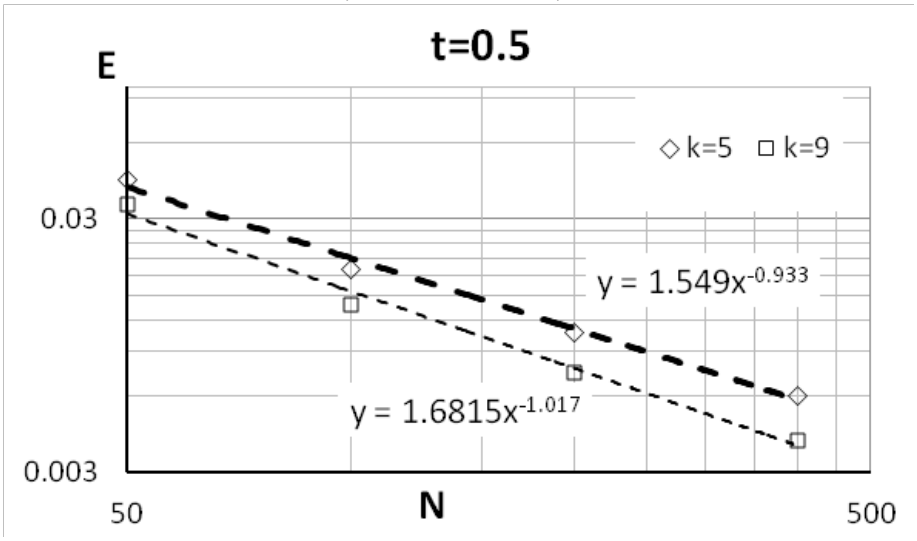

Fig. 7. Variation of E versus N for $k=5$ and $k=9$ at $t=0.5$. Dashed lines are the results of curve fitting.

The curve fitted formulas can be used to estimate the grid size N_9 needed to have the same error resulting from a grid N_5 . The error ratio is obtained as $E_5/E_9=\left(a_5 N_5{}^{b_5}\right)/\left(a_9 N_9{}^{b_9}\right)$, upon using Eq. (24) . Since we are seeking for the value of N_9 which yields the same error, the ratio E_5/E_9 is equated to 1.0 . Consequently the following formula is obtained for the grid ratio (GR):

$$GR=\frac{N_9}{N_5}=\left[\frac{a_5}{a_9}\left(N_5{}^{b_5-b_9}\right)\right]^{1/b_9} \tag{25}$$

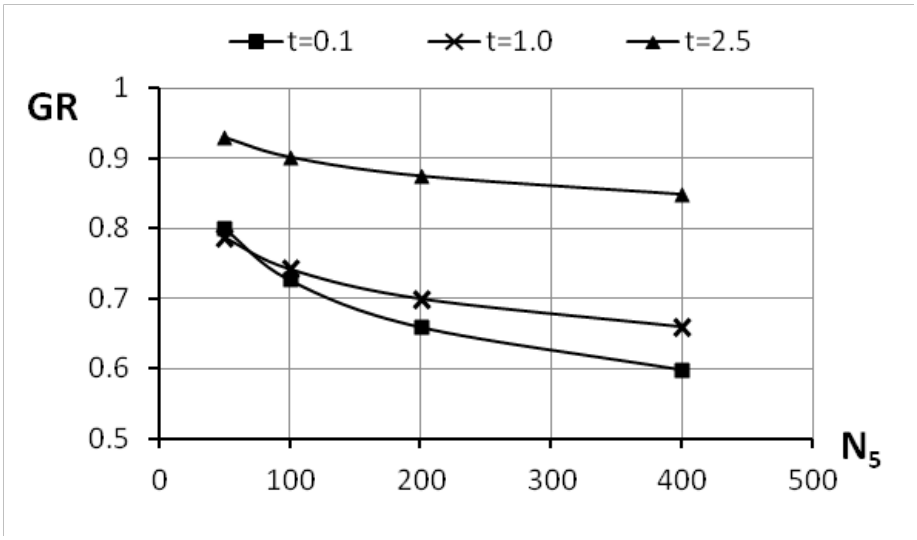

Fig. 8. GR versus N_5 for various values of t

The variation of GR versus N_5 is shown in Fig. 8 for different instants. Adopting a ninth order accurate scheme ($k=9$) is rather efficient at small values of t . For example at $t=0.1$ the

error resulting of adopting $N=400$ and $k=5$ is equal to that resulting from adopting $N=0.6\times400=240$ and $k=9$ ($1-GR=0.4\rightarrow40\%$ reduction in grid size). While for a relatively high value of $t=2.5$, GR is between 0.93 and 0.85 ($17\sim15\%$ reduction).

Case 2: Dirichlet Boundary Condition

In this section numerical results will be presented adopting a Dirichlet boundary condition. The space boundary conditions for temperature are identical to those described in the first problem, except at the left boundary, where a Dirichlet condition is imposed on the temperature

$$T(x=0,t)=1.0 \tag{26}$$

Zero initial conditions are assigned to T and $\partial T/\partial t$.
The exact solution of this problem is [6]:

$$\begin{gathered} T(x,t)=\frac{e^{\gamma t}}{t}\left[\frac{\bar{T}(x;\gamma)}{2}+\Re\left(\sum_{n=1}^{N}(-1)^n\bar{T}(x,\gamma+\frac{in\pi}{t})\right)\right] \\ \gamma=\frac{4.7}{t}\quad,\quad \bar{T}(x;p)=\frac{1}{p}\frac{\cosh\left[(1-x)\sqrt{p(1+Ve^2p)}\right]}{\cosh\left[\sqrt{p(1+Ve^2p)}\right]} \end{gathered} \tag{27}$$

Here $\Re(Z)$ is the real part of a complex number Z , and $i=\sqrt{(-1)}$.
Similar to the first problem, the symmetric nature allows imposing zero heat flux at the right boundary.

$$q(x=1,t)=0 \tag{28}$$

However imposing the correct boundary condition for q at the left boundary is not a trivial task. This condition should be specified to be consistent with the direction of propagation of information [2],[9]. At the left boundary W_2 should be extrapolated outside the domain. This extrapolated value should be used along with the prescribed temperature to calculate W_1 . In [2], Shen et al. used zero order extrapolation to estimate W_2 at the external nodes. While Yang in [9] adopted first order extrapolation by discretizing the second component of Eq. (10):

$$\frac{\partial W_2}{\partial t}-\frac{1}{Ve}\frac{\partial W_2}{\partial x}=\frac{q}{2Ve} \tag{29}$$

Yang approximated Eq. (29) using first order discretization in space and time:

$$\frac{{W_{2,0}}^{n+1}-{W_{2,0}}^{n}}{\Delta t}-\frac{1}{Ve}\frac{{W_{2,1}}^{n}-{W_{2,0}}^{n}}{\Delta x}=\frac{{q_0}^{n}}{2Ve} \tag{30}$$

The space derivative term $\partial W_2/\partial x$ is evaluated using down-winding as implied by the direction of propagation of W_2 (right to left). Once ${W_2}^{n+1}$ is obtained at the fictitious left boundary nodes, the relation $W_2=\frac{T}{2}-Ve\frac{q}{2}$ is used to obtain q using the prescribed value of T (Fig. 9). This first order method will be adopted in this study.

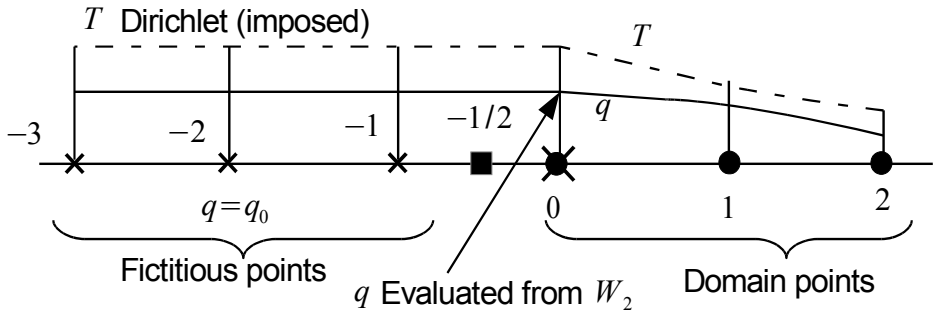

Fig. 9.Imposing boundary conditions at fictitious points for Dirichlet condition

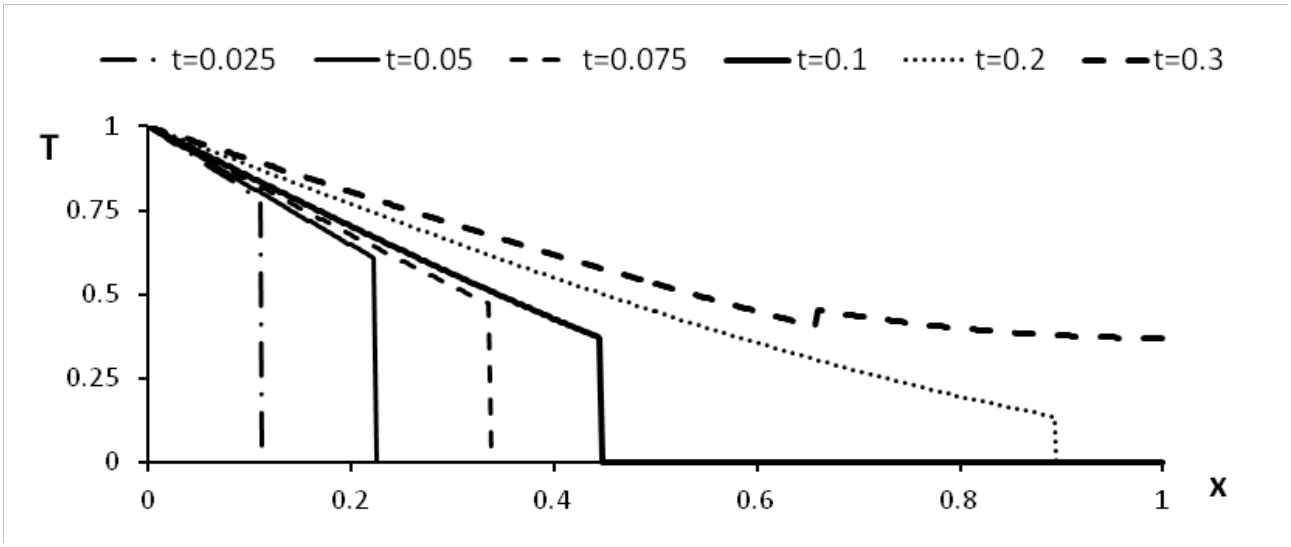

Fig. 10. Exact solution using Eq. (27) And adopting $Ve^2=0.05$

On Fig. 10 the exact solution is shown as calculated using Eq. (27) adopting $Ve^2=0.05$. The effect of the left Dirichlet boundary condition appears as shock traveling from left to right. The discontinuity across the shock is reduced with time due to the damping effects. The shock is reflected back after reaching the right boundary. The reflected shock appears as a relatively reduced space discontinuity in the temperature curve at $t=0.3$.

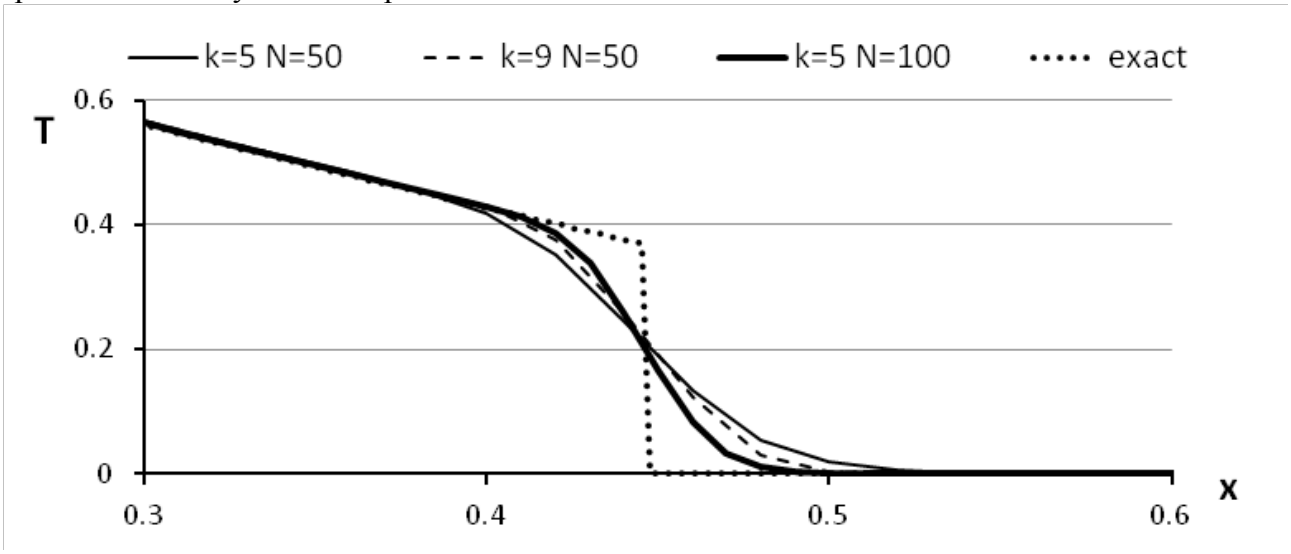

Fig. 11. Exact and numerical solutions at $t=0.1$

The spatial temperature distribution at $t=0.1$ is provided in Fig. 11. For the sake of comparison, the exact solution and the numerical solution adopting various orders ($k=5$ and 9) and grid

sizes ($N=50$ and 100), are shown. It should be noted that $\Delta t=0.1Ve/N$ for all simulations. It is obvious that the accuracy is proportional to both k and N . In addition spurious oscillations near the discontinuity are totally avoided.

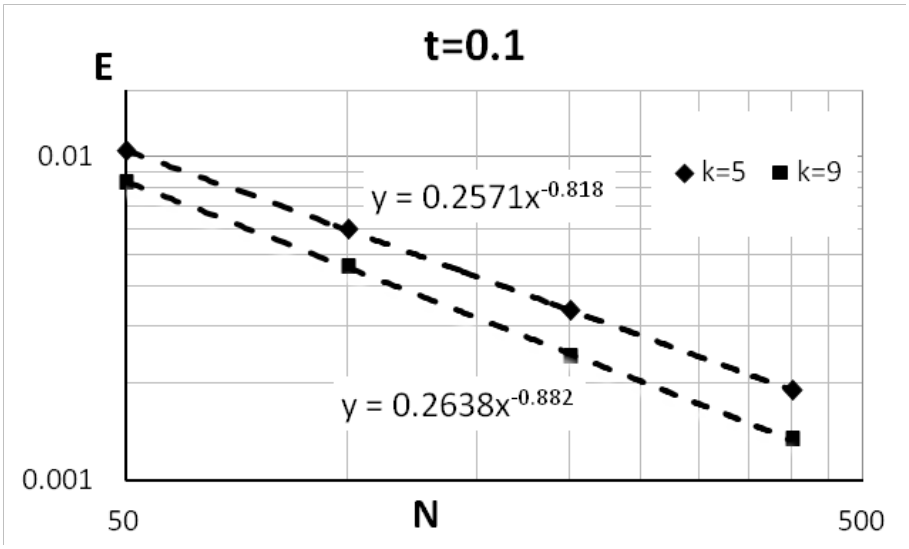

Fig. 12.Variation of E versus N for $k=5$ and $k=9$ at $t=0.5$ for case 2. Dashed lines are the results of curve fitting.

On Fig. 12 the relation between the error E and the grid size N is illustrated for different solution orders. Similar to the last problem Eq. (24) provides a good fit.

Finally The variation of GR versus N_5 is shown in Fig. 13 for various times. The grid reduction is higher for relatively small values of $t\in[0.025\,,0.1]$. However for higher values of $t\sim 0.2$, the grid ratio increases $GR\sim 0.8$ and the gain of increasing k decreases. In fact the exact solution predicts a continuous damping of the sharp gradients as time increases. For these instants the solution is relatively smooth and the order of the numerical method may become less important.

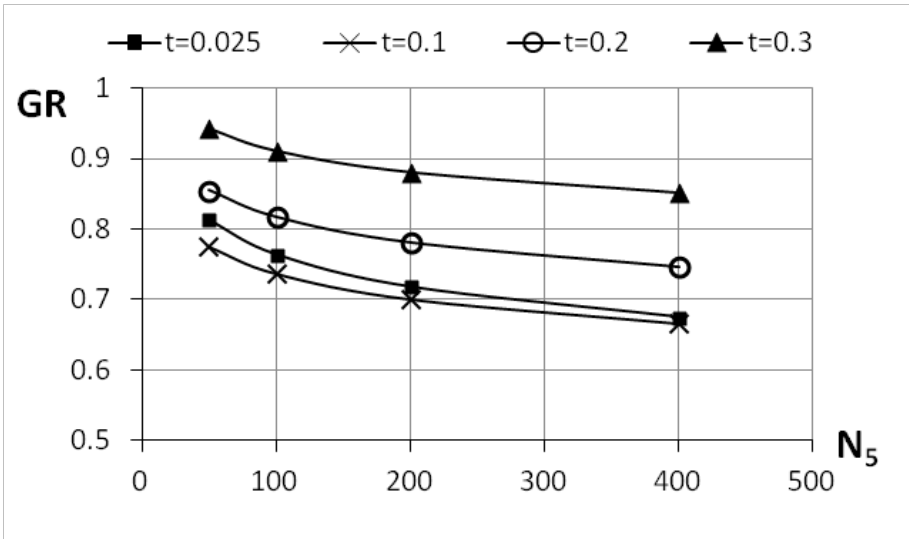

Fig. 13. GR versus N_5 for various values of t for case2

These observations agree well with those obtained from the results of case 1. It should be noted that relatively high order discretization was adopted at the boundaries for case1. While low order discretization (first order) was adopted in the case 2. It is interesting to note that this difference does not have a strong effect on the solution characteristics.

Finally, the common features between the results of both cases provide further validation for our findings.

5. Conclusions

In this paper hyperbolic heat conduction has been simulated using high order space accurate WENO method. The numerical results were validated via comparison with exact solutions. The sharp gradients which characterize the hyperbolic model are captured accurately and spurious oscillations are avoided. The accuracy of the model is verified to be proportional to the number of grid points and the order of the numerical algorithm.

In order to clarify the treatment of the wide stencil near boundaries two cases of different boundary conditions (Dirichlet and Neumann) were analyzed. Algorithms to assign values at external fictitious grid points were provided. The Dirichlet case is relatively complicated since the boundary conditions should be assigned consistently with the problem characteristics field. Although relatively low order (first order) boundary condition was used for Dirichlet case, the numerical behavior of the error is rather similar for both cases.

In order to quantify the gain of increasing the order of the numerical method, the error was presented for various instants and adopting various grid sizes. As expected less number of grid points are needed by a ninth order method to achieve the same accuracy of a fifth order method. The ratio between the number of grid points of ninth and fifth order methods was always less than 1.0 . However this ratio was relatively low (~60%) in the transient periods, compared to the steady periods (~90%) . This may be attributed to the presence of relatively sharp gradients in the transient interval. The quantitative analysis presented shows that the ~50% reduction reported by [11] may be unrealistic for some cases, especially those characterized by relatively smooth steady solutions.

The results of the current study provide motivation for extending the work to multidimensional problems and for even higher order numerical methods. Another possible extension would be exploring the behavior of other methods including the Discontinuous Galerkin finite element. The authors plan to study these topics in the near future.

References

[1] D.Y. Tzou, Computational techniques for microscale heat transfer, Handbook of Numerical Heat Transfer, Editors: W.J. Minkowycz, E.M. Sparrow, J.Y. Murthy, John Wiley & Sons, (2006) 623-657.

[2] W. Shen, L. Little, L. Hu, Anti-Diffusive methods for hyperbolic heat transfer, Computer Methods in Applied Mechanics and Engineering 199 (2010) 1231-1239.

[3] Y. Chou, R. J. Yang, Application of CESE method to simulate non-Fourier heat conduction in finite medium with pulse surface heating, International Journal of Heat and Mass Transfer 51 (2008) 3525-3534.

[4] X. Ai, B.Q. Li, A discontinuous finite element method for hyperbolic thermal wave problems, Engineering Computations 21 (2004) 577-597.

[5] G.F. Carey, M. Tsai, Hyperbolic heat transfer with reflection, Numerical Heat Transfer 5 (1982) 309-327.

[6] D.Y. Tzou, A unified field approach for heat conduction from macro- to micro-scales, Journal of Heat Transfer 117 (1995) 8-16.

[7] A. Moosaie, Non-Fourier heat conduction in a finite medium with insulated boundaries and arbitrary initial conditions, International Communications in Heat and Mass Transfer 35 (2008) 103-11.

[8] C.W. Shu, Essentially non-oscillatory and weighted essentially non-oscillatory schemes for hyperbolic conservation laws, Advanced Numerical Approximation of Nonlinear Hyperbolic Equations, Editors: Quarteroni, Springer, (1998) 325-432.

[9] H.Q. Yang, Characteristics-based, high-order accurate and nonoscillatory numerical method for hyperbolic heat conduction, Numerical Heat Transfer, Part B 8 (1990) 221-241.

[10] D.S. Balsara, C.W. Shu, Monotonicity preserving weighted essentially non-oscillatory schemes with increasingly high order of accuracy, Journal of Computational Physics 160 (2000) 405-452.
[11] J. Shi, Y.T. Zhang, C.W. Shu, Resolution of high order WENO schemes for complicated flow structures, Journal of Computational Physics 186 (2003) 690-696.
[12] S.T. Miller, R.B. Haber, A spacetime discontinuous Galerkin method for hyperbolic heat conduction, Computer Methods in Applied Mechanics and Engineering 198 (2008) 194-209.
[13] J.A. Ekaterinaris, High-order accurate, low numerical diffusion methods for aerodynamics, Progress in Aerospace Sciences 41 (2005) 192-300.
[14] G.A. Gerolymos, D. Senechal, I. Vallet, Very-high-order WENO schemes, Journal of Computational Physics 228 (2009) 8481-8524.
[15] J.A. Trangenstein, Numerical Solution of Hyperbolic Partial Differential Equations, Cambridge University Press, (2007) .